Applied Physics A (2018) 124:744
https://doi.org/10.1007/s00339-018-2151-y

Applied Physics A
Materials Science & Processing

Optical and microelectronic analysis of rhodamine B-based organic Schottky diode: a new trend application

G. F. Salem[1] · E. A. A. El-Shazly[1] · A. A. M. Farag[1,2] · I. S. Yahia[3,4,5]

Received: 24 June 2018 / Accepted: 1 October 2018

Abstract
The spin-coating technique was effectively used to prepare a good adherent and uniform thin films of rhodamine B (Rh.B). The investigation of the optical absorption revealed indirect energy gap of 2.1 eV and Urbach energy of 29 meV. The investigation of the electrical characteristics of the heterojunction-based Rh.B was achieved to extract the important parameters and identify the predominant conduction mechanism. Dark forward and reverse biasing current density–voltage characteristics showed notable rectification characteristics. The heterojunction conduction mechanism of Rh.B/p-Si confirms that observed mechanisms depend on the applied voltage range. The capacitance–voltage characteristics, measured at different signal frequencies, indicated the occurrence of an abrupt type of heterojunction. The frequency dependence of some heterojunction parameters like barrier height, maximum electric field, the width of the depletion region, and carrier concentration gives an indication for the type of interfacial layer of the heterojunction. A high dependence of the capacitance and conductance on both the biasing voltage and the applied frequency was observed. Moreover, the measured series resistance emphasizes the strong effect on the extracted parameters of the studied Schottky diode. Rh.B-based Schottky diode is a promising for multi-applications in an electronic device.

1 Introduction

Organic semiconductors are promising materials in wide-scale electronic and optoelectronic devices [1, 2]. Scientists and engineering make a lot of new progress in the device technology with their studying their electronic properties [1–3]. Organic substances own specific optical and electrical characteristics suitable for enormous applications [2, 3]. The most important features of organic materials are the easy fabrications process using low-cost technology even by thermal evaporation in comparison with inorganic materials [4]. Organic, flexible technology is the main goals for the new industrial for flexible devices [4, 5]. Nowadays, organic material has a spread market for new applications such as an organic light-emitting diode (OLED), batteries, computer boards, laser printers, copy machine, solar cell devices, dye-sensitized solar cells,…etc. [6–11].

Rhodamine B is an organic laser dye and can be used in different applications in physics, chemistry and biotechnology [12]. Farag et al. [13] studied the optical constants of Rh.B on glass substrates, and they calculated the optical constant with their optical parameters such as refractive index, absorption index, band gap and dielectric properties. The band gap of Rh.B is determined as 1.97 eV with phonon energy of 75 meV. In addition, Farag et al. [14] investigated the Schottky diode of Rh.B using ohmic and Schottky contacts and they found that Rh.B possess a Schottky behavior with a rectification values 636 at 0.15 V. In addition, other parameters of the Schottky diode were obtained such

✉ A. A. M. Farag
alaafaragg@gmail.com; aamfaraj@ju.edu.sa; alaafaragg@edu.asu.edu.eg

[1] Thin Film and Solar Cells Laboratory, Physics Department, Faculty of Education, Ain Shams University, Cairo 11757, Egypt

[2] Physics Department, Faculty of Sciences and Arts, Jouf University, Jouf, Saudi Arabia

[3] Research Center for Advanced Materials Science (RCAMS), King Khalid University, P.O. Box 9004, Abha 61413, Saudi Arabia

[4] Advanced Functional Materials and Optoelectronic Laboratory (AFMOL), Department of Physics, Faculty of Science, King Khalid University, P.O. Box 9004, Abha, Saudi Arabia

[5] Nanoscience Laboratory for Environmental and Bio-Medical Applications (NLEBA), Semiconductor Lab., Metallurgical Lab., Physics Department, Faculty of Education, Ain Shams University, Roxy, Cairo 11757, Egypt

Published online: 10 October 2018

as ideality factor, barrier height, saturated density current, carrier concentration and Fermi level potential. The laboratory analysis of Schottky diode parameters attains the barrier height inhomogeneities of the Rh.B Schottky diode [13, 14].

In this communication, the preparation and characterization of Rh.B thin film- based heterojunction were studied. The main important parameters that control the heterojunction performance like rectification factor, barrier height, series and shunt resistances were extracted from the forward current–voltage characteristics. In addition, the prevalent mechanisms of conduction were considered. Furthermore, frequency and bias dependences of the capacitance and conductance and their related parameters were also investigated.

2 Experimental details

Rhodamine B was obtained from Sigma-Aldrich Company without refinement. P-Type Si wafer was cleaned by diluted nitric acid, diluted hydrochloric acid and ethanol to remove any native oxide on both side of the silicon wafer. A stream of nitrogen gas was utilized to dry the silicon wafer. Aluminum back contact was deposited on the one side of the silicon wafer using thermal evaporation machine (Edwards 306-A) under base pressure of 1.5×10^{-4} Pa. After that, the Al/p-Si was annealed for 5 min at 450 °C to allow the aluminum to be diffused inside the silicon to make the ohmic contact. The other surface of the Si wafer was cleaned again by the same method, discussed above, to remove any metal oxide formed during the annealing process. 10^{-2} M of Rhodamine B soluble in ethanol was formed using a magnetic stirrer at room temperature. Homemade design spin-coating system was used to deposit Rh.B on highly cleaned p-Si/Al at 1500 rpm for 60 s. After that point contact from gold (Au) using specially designed mask was deposited on Rh.B/p-Si/Al to form the top metal contact using sputtering system model (Denton Vacuum DV502A DC sputtering system). The Rh.B thin film of 120 nm was deposited by spin-coating system at 1500 rpm. The aluminum thickness layer is controlled to be about 100 nm, while the gold thickness layer is about 30 nm. The *I–V* and *C–V* characteristics were recorded using a semiconductor characterization system 4200-SCS at room temperature. Two pre-amplifiers were used to connect the Teflon/copper metal holder to measure both *I–V* and *C–V* at room temperature.

3 Results and discussion

3.1 Molecular parameters characterizations

The molecular structure of RH.B using Chem 3D Pro 10.0 is shown in Fig. 1. The crystalline structure of the Rh.B films,

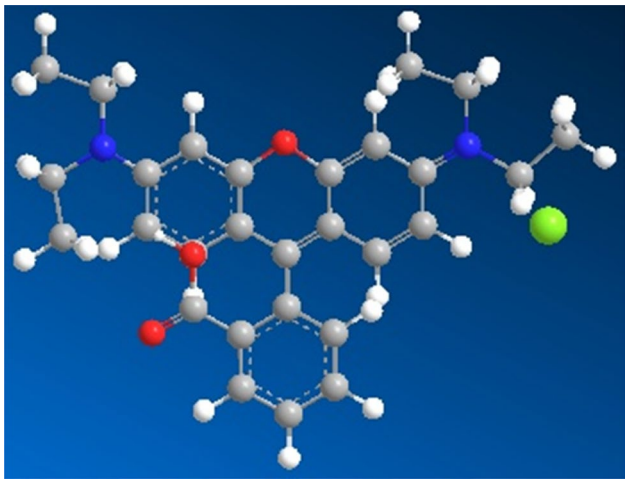

Fig. 1 Rhodamine B using Chem 3D Pro 10.0

deposited on a glass substrate at 300 K is examined by the X-ray diffraction and is illustrated in Fig. 2a. The pattern shows indistinct structures with a wide broad hump which characterizing the short-chain ordering crystalline structure (amorphous). This result is supported by those obtained from the selected area electron diffraction image (SAED), as shown in Fig. 2b. Another result can be obtained from the TEM image which indicates a very fine and/or dust-like structure with nanostructure sizes (not shown here). The particle size distribution is obtained and is illustrated in Fig. 2c. Accordingly, the mean value of the particles is around 3 nm which with those published in the literature [13].

The acquired theoretical calculation of HOMO and LUMO structures of Rh.B at DFT/B3LYP/6-311G** utilizing DFT is shown in Fig. 3. The fundamental atomic parameters such as energy gap ($E_{\mathrm{HOMO-LUMO}}$), ionization potential (I_p), electron affinity (EA) and softness (S) were resolved utilizing the hypothetical examinations and relations discussed in details elsewhere [15]. These parameters are utilized for affirming the stabilization and reactivity of the Rh.B and are recorded in Table 1.

3.2 Optical absorption characteristics of Rh.B thin films

The Rh.B thin film shows a high absorption coefficient ($\alpha > 10^4$ cm^{-1}) in the visible region, as well as a sharp edge at 600 nm, which support the probability for the optoelectronic application. Furthermore, the energy band gap (E_g) of Rh.B films is resolved according to the relation of $(\alpha h\nu)^{1/2}$ vs. $(h\nu)$ plot. A straight line fitting part of the plot is obtained, as shown in Fig. 4a, confirming the presence of indirect allowed transition with an energy gap of 2.1 eV. The experimental energy band gap of RHB film is found to be lower than those obtained using the theoretical calculation

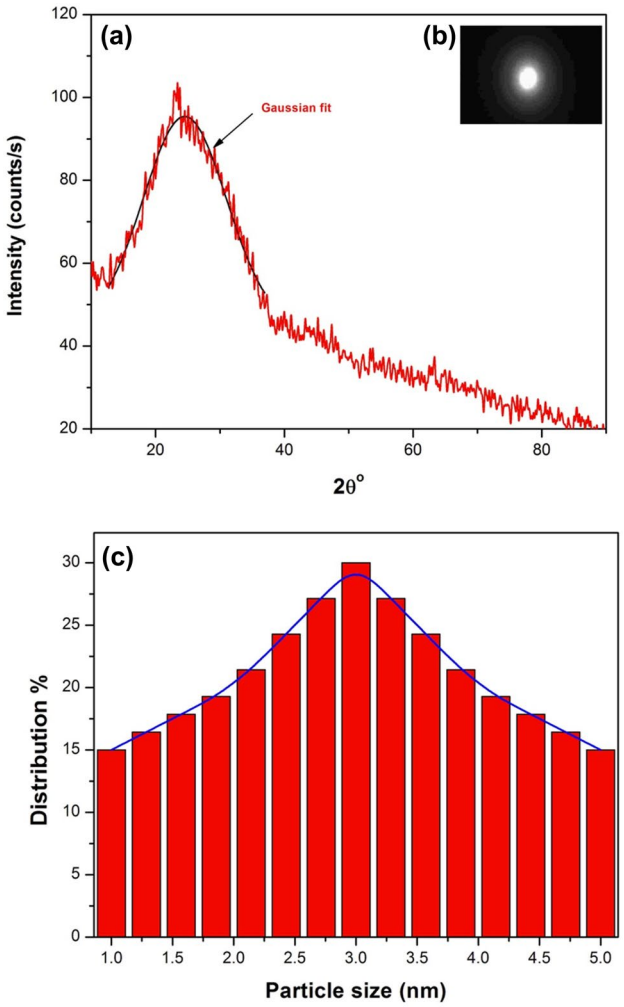

Fig. 2 **a** XRD pattern, **b** SAED image, and **c** plot of particle size distribution of Rh.B

at DFT/B3LYP/6-311G** utilizing DFT (i.e., 2.6 eV). The change between the two calculations can be due to that the theoretical calculations considered the single molecule in its application (i.e., gaseous state), in contrast to the experimental one.

The observed absorption region is related to the interband transitions through the band tails in the energy gap of Rh.B. Accordingly, the absorption coefficient follows the relation [16], $\alpha = \alpha_0 \exp\left(\frac{h\nu}{E_u}\right)$, where α_0 and E_u are, respectively, the pre-exponential factor and Urbach energy which related to the width of the band tails of the localized states. The Urbach energy is determined from the inverse slope of the straight line fitting of the $\ln(\alpha) - h\nu$ plot (Fig. 4b) and found to be 29 meV. The width of the band tail is probably caused by the structural randomness due to the presence of defects, impurities and dislocated crystallites [17].

3.3 Current density–voltage characteristics of Rh.B-based organic Schottky diode

The schematic diagram of Au/Rh.B/p-Si/Al heterojunction (HJ) diode is illustrated in Fig. 5. The measurements of *I–V* were utilized to obtain the information about the current mechanism and obtaining the prime essential parameters [18]. Figure 6a shows the dark *I–V* measurements of Rh.B/p-Si HJ at 300 K. As observed, the heterojunction yielded good rectifying property, and the room temperature rectification ratio is calculated and plotted as a function of voltage, as evident in Fig. 6b. This property confirms the diode-like behavior due to the formation of the barrier at the heterojunction interface that limits the flow of the forward and reverses carriers [19]. In addition, increasing the RR values

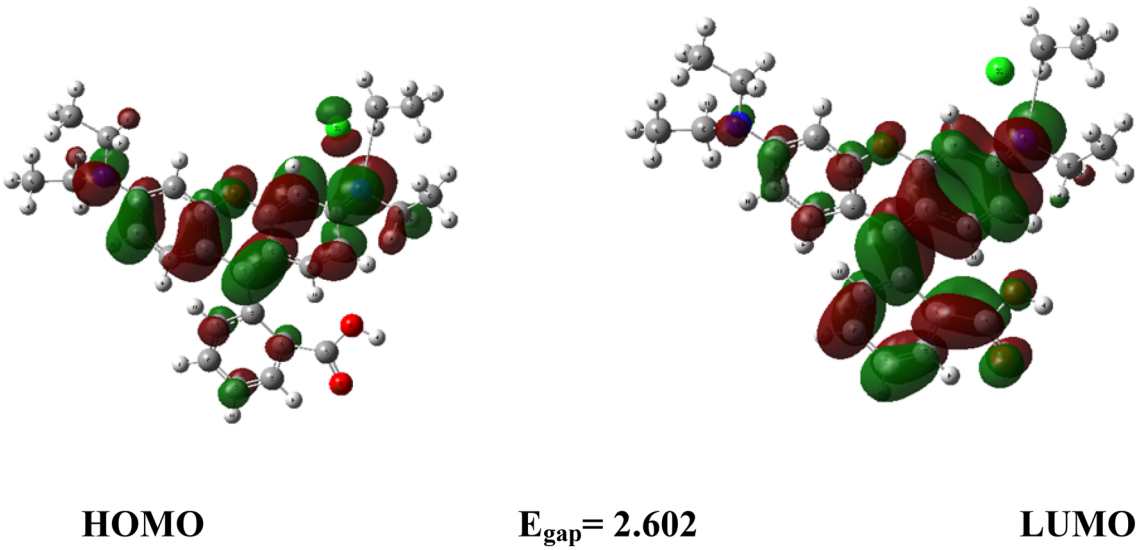

Fig. 3 HOMO–LUMO gap of Rh.B

Table 1 HOMO–LUMO parameters calculated for Rh.B at DFT/B3LYP/6-311G**

Structure	E_{HOMO} (eV)	E_{LUMO} (eV)	E_g (eV)	I_p (eV)	EA (eV)	S (eV)
RhB	− 5.666	− 3.064	2.602	5.666	3.064	0.768

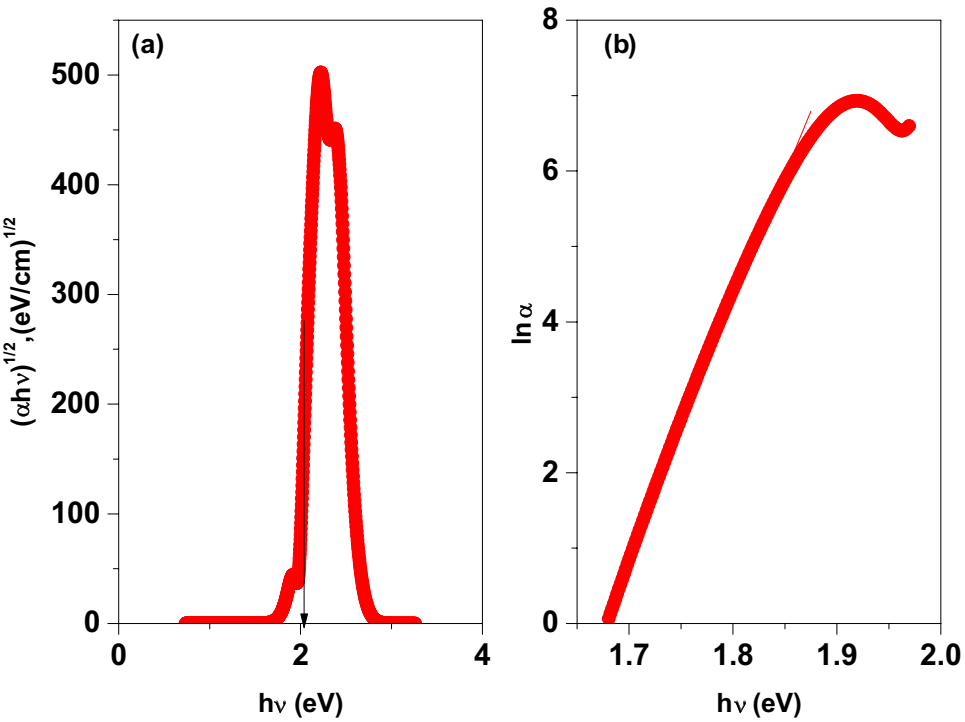

Fig. 4 **a** Plot of $(\alpha h\nu)^{1/2}$ vs. $h\nu$ and **b** plot of lnα vs. $h\nu$ of Rh.B thin films

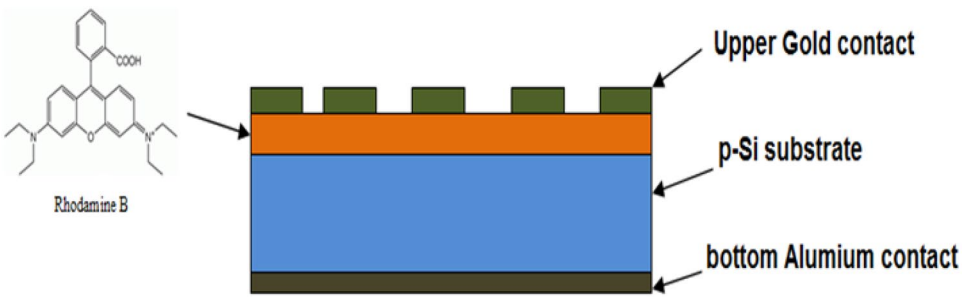

Fig. 5 Schematic diagram of Au/Rh.B/p-Si/Al heterojunction diode

with increasing the applied voltage means an enhancement in the heterojunction characteristic which can be considered promising for different electronic applications. Accordingly, the current density–voltage characteristics of the heterojunction, using the thermionic emission theory can be expressed as follows [20]:

$$J = J_0\left(\exp\frac{q(V - JR_s)}{\eta kT} - 1\right) + \left(\frac{V - JR_s}{R_{sh}}\right), \quad (1)$$

where J_0 is the reverse saturation current density, η is the ideality factor, k is the Boltzmann's constant, T is the absolute temperature, q is the electronic charge, R_s is the series resistance and R_{sh} is the shunt resistance. Semi-logarithmic plot of the room temperature current–voltage (I–V) characteristics of Rh.B/p-Si heterojunction is clarified in Fig. 7a. The values of R_{sh} and R_s can be approximated from the graphical representation of I–V under low and high forward bias, respectively. Values of R_s and R_{sh} were estimated from the graphical representation of the junction resistance R_J vs. applied voltage, as Fig. 7b and listed in Table 2. A higher value of the series resistance, as compared with those published for organic-based diodes [14, 21–24], can be attributed to the higher value of Rh.B bulk resistance and some resistances originated from the heterojunction contact.

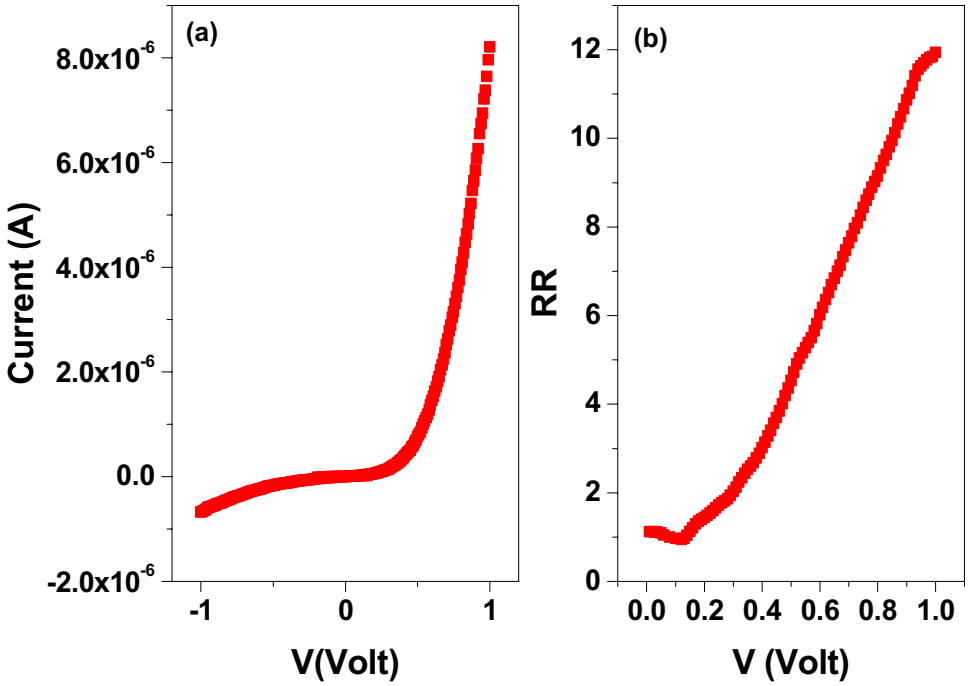

Fig. 6 **a** Plot of I vs. V and **b** plot of RR vs. V for Rh.B/p-Si heterojunction

Table 2 Main extracted parameters from current–voltage characteristics of Rh.B/p-Si heterojunction

	Extracted from I–V characteristics			Extracted from dV/dln$I$		References
	η	R_s (Ω)	R_{sh} (Ω)	η	R_s (Ω)	
Au/Rh.h/p-Si/Al	2.5	1.5×10^5	5.3×10^6	1.6	5.53×10^3	Present work
Al/Rh.B Schottky diode	1.57	210	–	–	–	[14]
Al/SCC/ITO	1.73	2.32×10^3	–	–	–	[21]
Al/NPC/ITO	2.42	13×10^3	–	–	–	[22]
Zn[$((NO_2)_2$-8HQ$)_2$] complex film/n-Si	7.2	50×10^3	–	–	–	[23]
Au/PPy/n-Si Schottky barrier diodes	5.41	10^3	130×10^6	–	–	[24]

In addition, the higher value of the shunt resistance can be explained by the lower leakage current through the heterojunction [25–28]. It is well known that for the perfect diode, R_s and R_{sh} tend to zero and infinity, respectively [20].

Another methodology can be used for determining some important heterojunction parameters such as the ideality factor and the series resistance stated by Khusayfan et al. [29]. This method based on Cheung and Cheung formula as follows [30, 31]:

$$\left(\frac{dV}{d\ln J}\right) = JR_s + \eta\left(\frac{kT}{q}\right). \quad (2)$$

Accordingly, the plot of $\left(\frac{dV}{d\ln J}\right)$ vs. J can be used for extracting R_s from the slope and η the intercept at $J=0$, as shown in Fig. 8a. The obtained values of R_s and η are found to be 5.533×10^3 Ω and 1.6, respectively. The extracted R_s and η are relatively lower than those obtained above due to the applied voltage range dependence [29]. Another explication can be acquired by Phark et al. [32]. They have explained that the uniform the non-uniform dispersion of the surface microstructures may prompt an inhomogeneous barrier height. Moreover, Werner and Guttler [33] have suggested that the barrier height inhomogeneity can be clarified by postulating a Gaussian distribution of the Schottky with considering a mean barrier height and a standard deviation.

The logarithmic plot of the forward current–voltage characteristics of the heterojunction is shown in Fig. 8b. This plot has two different linear distinct regions depending on the applied voltage, which is represented as a region (I) and region (II) due to the probability of two distinctive prevailing mechanisms. Accordingly, the current density with the applied voltage follows the well-known relation, $I\ \alpha\ V^m$, where m is the exponent that used for realizing the type of the predominating mechanism. Values of m

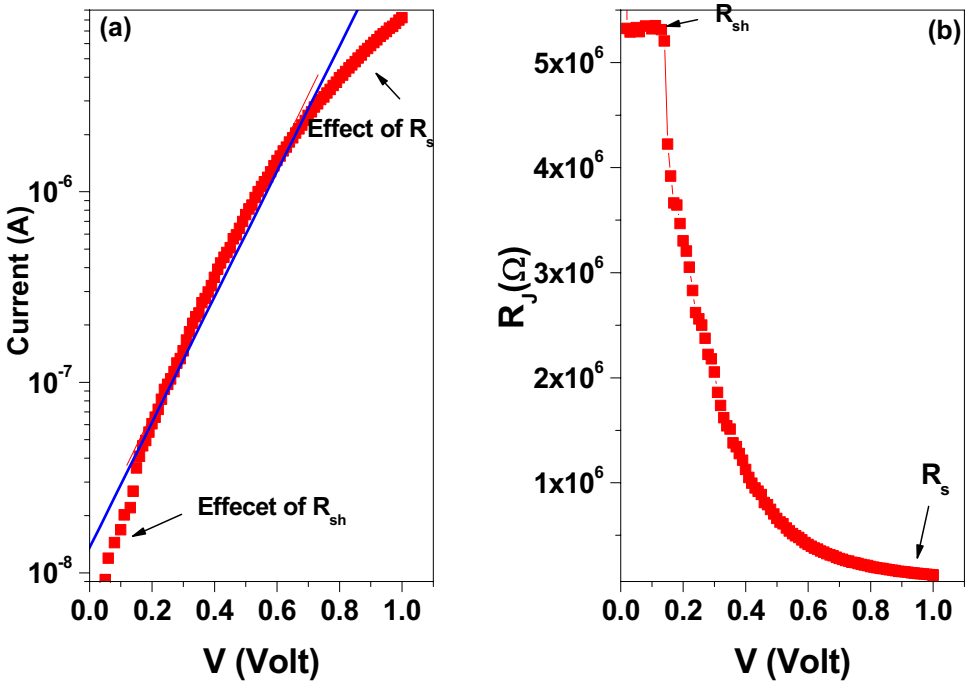

Fig. 7 **a** Plot of current, I vs. V and **b** plot of R_J vs. V for Rh.B/p-Si heterojunction

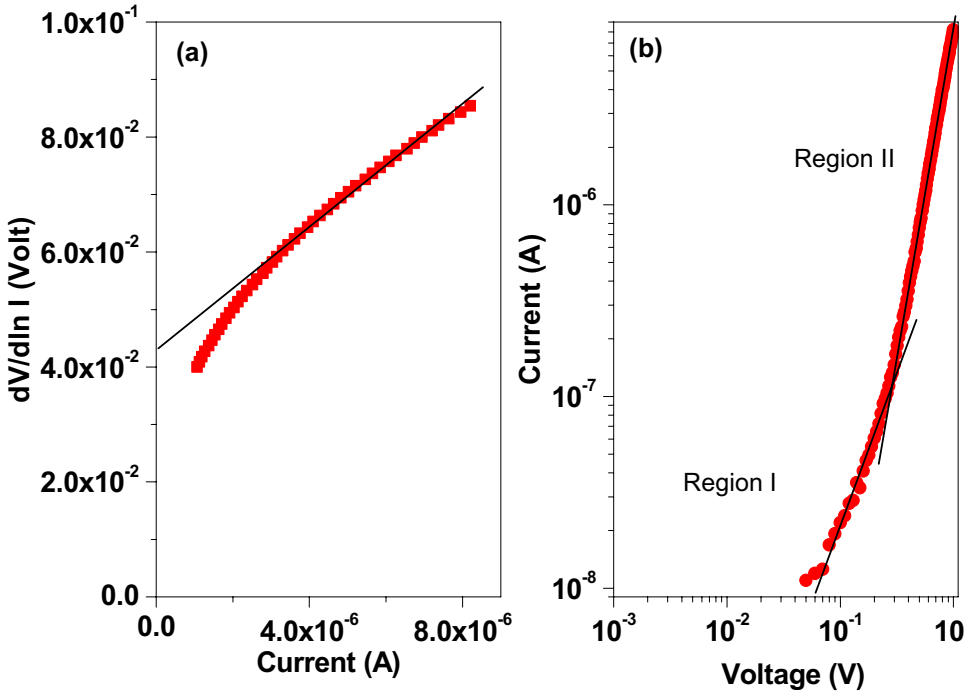

Fig. 8 **a** Plot of dV/dln$I$ vs. current, I and **b** plot of current, I vs. V for Rh.B/p-Si heterojunction

for regions (I and II) are found to be ~2 and ~3, corresponding to the trap-free square-law region and the exponential trap distribution [34, 35]. The acquired results are recorded in Table 3 in comparison with other published organic-based devices [36, 37]. The results confirmed the presence of space charge conduction with exponential distribution at higher potential, while at the lower potential, the mechanism is a free trap with the square law or ohmic law behavior.

The existence of space charge limited conduction gives an indication for presence one contact has high injecting properties to supply an unfailing source of carriers [38, 39]. In region (I), it is expected that the number of thermally excited carriers are unsuitable, and then trap levels are nearly

Table 3 Value of the slope and their corresponding mechanisms from the current–voltage characteristics of Rh.B/p-Si heterojunction

Structure	m_1	Type of mechanism in (Region I)	m_2	Type of mechanism in (Region II)	References
Au/Rh.h/p-Si/Al	2	Trap-free square-law region	3	Exponential trap distribution	Present work
Au/PPy/n-Si Schottky barrier diode	1.97	Ohmic behavior	3.88	SCLC	[36]
Al/CuPc/n-Si device	2	SCLC controlled by single dominating trap level	3	Exponential trap distribution	[37]

empty. With increasing the applied voltage, the density of injected carriers increase and then dominating the charge-carrier transport to the limit of trap filling [40]. It is well known that the space charge limited conduction mechanism at which the current is limited, while applied electric field is controlled by the field due to space charge [41–43].

3.4 Frequency and biasing voltage dependence of *C–V* and *G–V* characteristics

The characteristics of both capacitance–voltage and conductance–voltage of Rh.B-based heterojunction are measured in a wide frequency range from 2 kHz to 10 MHz at 300 K and are given in Figs. 9a–d and 10a–c, respectively. Obviously, both capacitance and conductance are found to be dependent on the biasing voltage and the applied frequency. In addition, the value of capacitance and conductance are found to decrease with increasing the frequency signal due to the probability for the presence of heterojunction interface. At the lower frequency's region, the interface can undergo the AC signal and produce an additional capacitance, which displays frequency dependence due to the time of relaxation of the carriers at the interface. While at enough higher frequencies the interface charges can barely undergo the AC signal and then a neglecting of the interface states capacitance contribution to the overall capacitance is taken place. In addition, the measured capacitance and conductance are dependent on the biasing

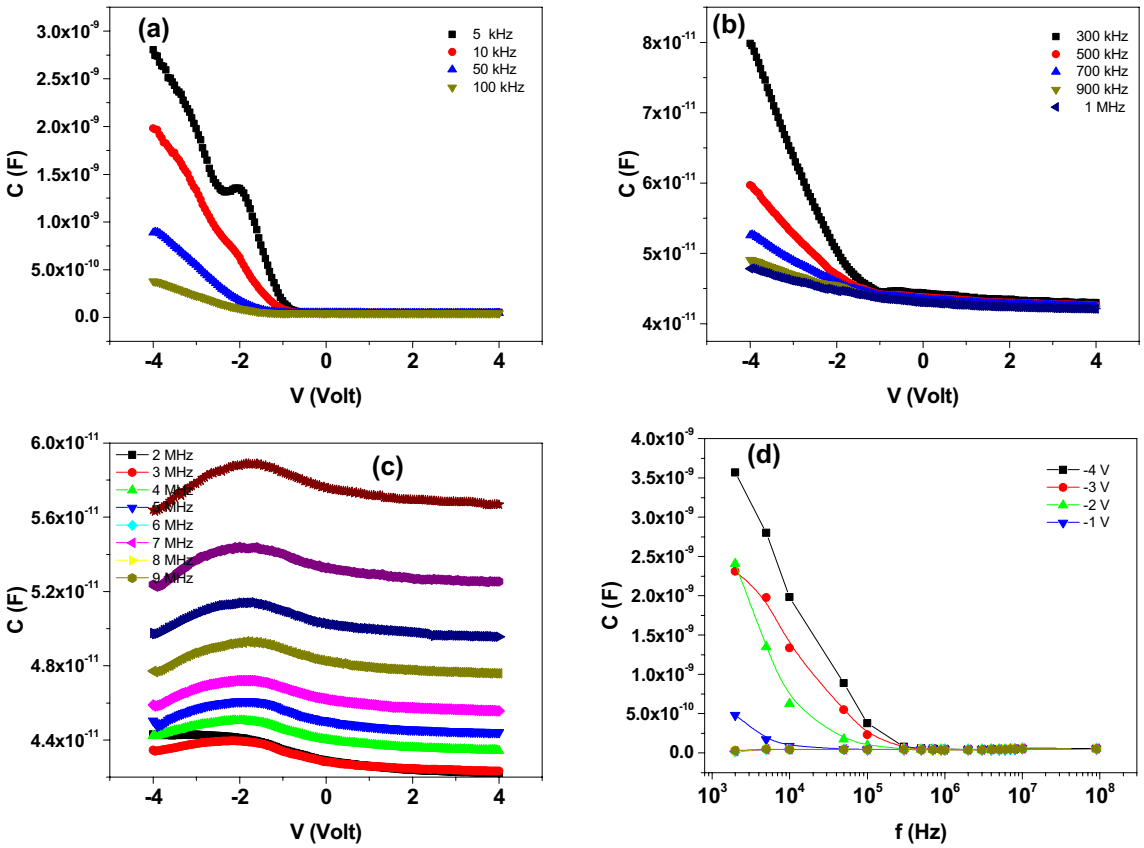

Fig. 9 **a–c** Plots of capacitance, *C* vs. *V* at different frequency ranges, **d** plot of capacitance, *C* vs. *f* for Rh.B/p-Si heterojunction

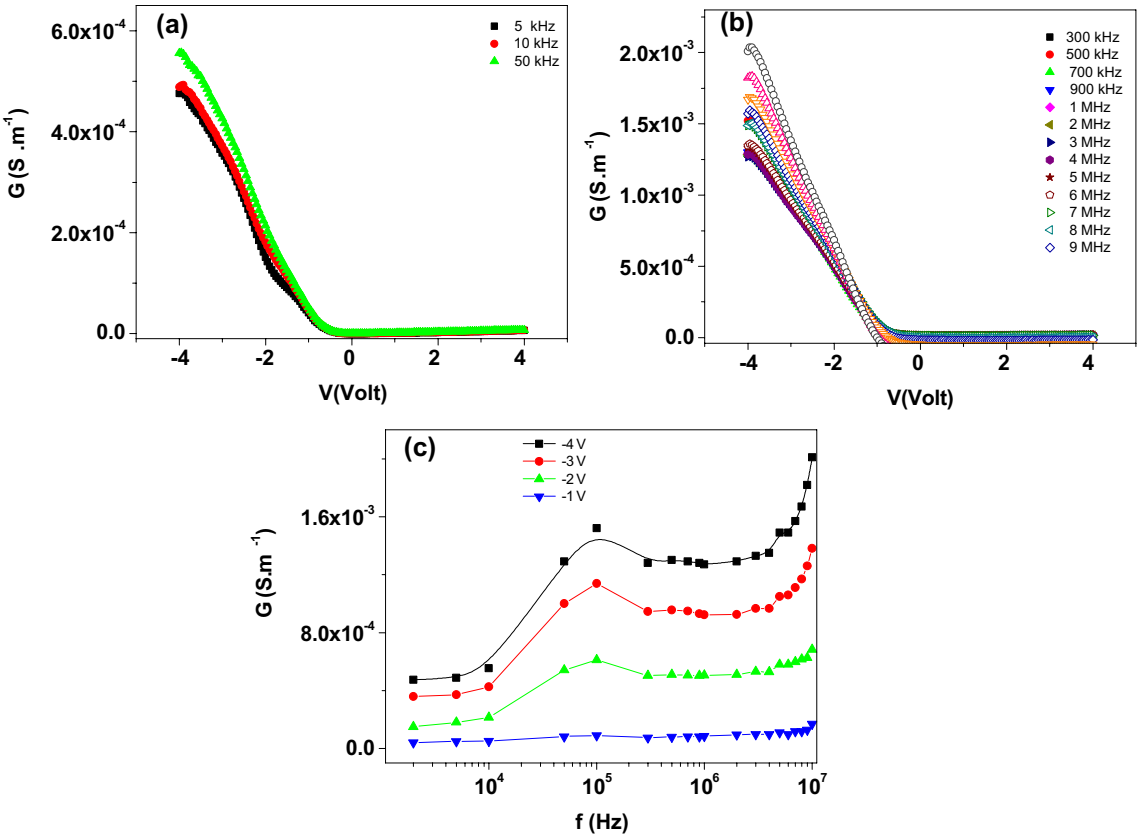

Fig. 10 **a, b** Plots of conductance, G vs. V at different frequency ranges. **c** Plot of conductance, G vs. f for Rh.B/p-Si heterojunction

voltage. Moreover, a decreasing of capacitance, whereas increases in the conductance as the frequency increases at certain applied voltage are shown in Figs. 9d and 10c, respectively. Furthermore, a near saturation for the capacitance is taken place at forwarding bias, which is recognized as an accumulation region, as shown in Fig. 9d. R_s of the Rh.B/p-Si heterojunction can be determined from both capacitance and conductance values using the following expression as stated by Nicollian's and Goetzberger's [42]:

$$R_s = \frac{G}{G^2 + (\omega C)^2}. \tag{3}$$

Figure 11a–d shows a high dependence of the series resistance on both biasing voltage and the applied frequency signal. It is also observed, a characteristic peak is observed for the behavior of series resistance at a certain applied voltage, especially at the lower frequency range, where the interface states has a high influence, and the value of the series resistance was decreased with increasing the AC field and the situation of the maxima shifts toward the negative biasing voltage region [43, 44], as shown in Fig. 11d. Bülbül and Zeyrek [45] have attributed this behavior to the re-structure for the semiconductor under the effect of applied voltage at different frequenices.

Determination of some important parameters from the capacitance–voltage characteristics of Rh.B/p-Si heterojunction at different frequencies. Frequency dependence for plots of $1/C^2$–V characteristics under the effect of various frequencies is shown in Fig. 12a. These plots have a significantly fitting linear portion which supports the abrupt type for the studied heterojunction at each frequency. Whereby, though the linearity of $1/C^2$–V plots, a little contribution of the interface states and excess capacitance may be realized through the C–V measurements [46]. Goodman [47] have reported that the real value of the barrier height can be estimated from the linear intercept of the graphical representation of V_{cutoff} vs. ω^2 to zero frequency, as represented in Fig. 13b. A linear fit representation is observed, and the obtained value is lower the reported energy gap of Rh.B thin films but incomparable with those for Si-single crystal [48]. Accordingly, the capacitance–voltage characteristics by ignoring the influence of the voltage drop causing by the presence of interfacial states can be specified by the following relation [49]:

$$\frac{1}{C^2} = \left(\frac{2}{q\varepsilon\varepsilon_0 A^2 N}\right)(V_b + V), \tag{4}$$

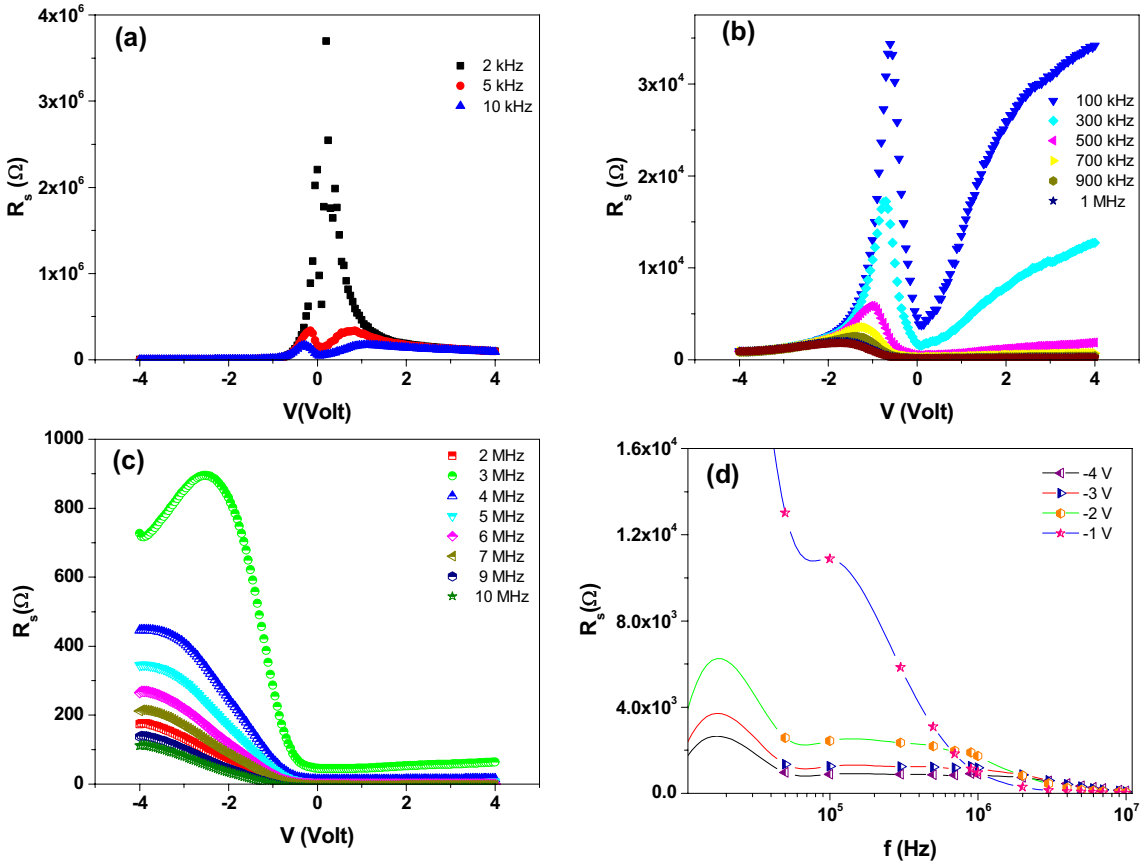

Fig. 11 **a**–**c** Plots of series resistance, R_s vs. V at different frequency ranges. **d** Plot of series resistance, R_s vs. f for Rh.B/p-Si heterojunction

Fig. 12 **a** Plot of $1/C^2$ vs. f and **b** plot of V_{cutoff} vs. ω^2 for Rh.B/p-Si heterojunction

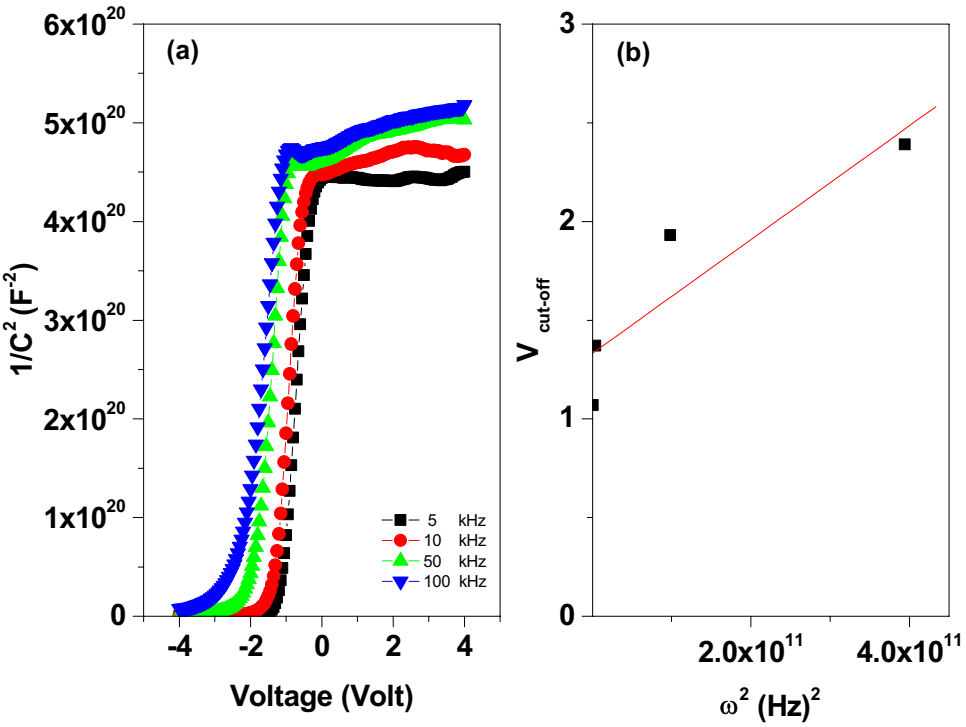

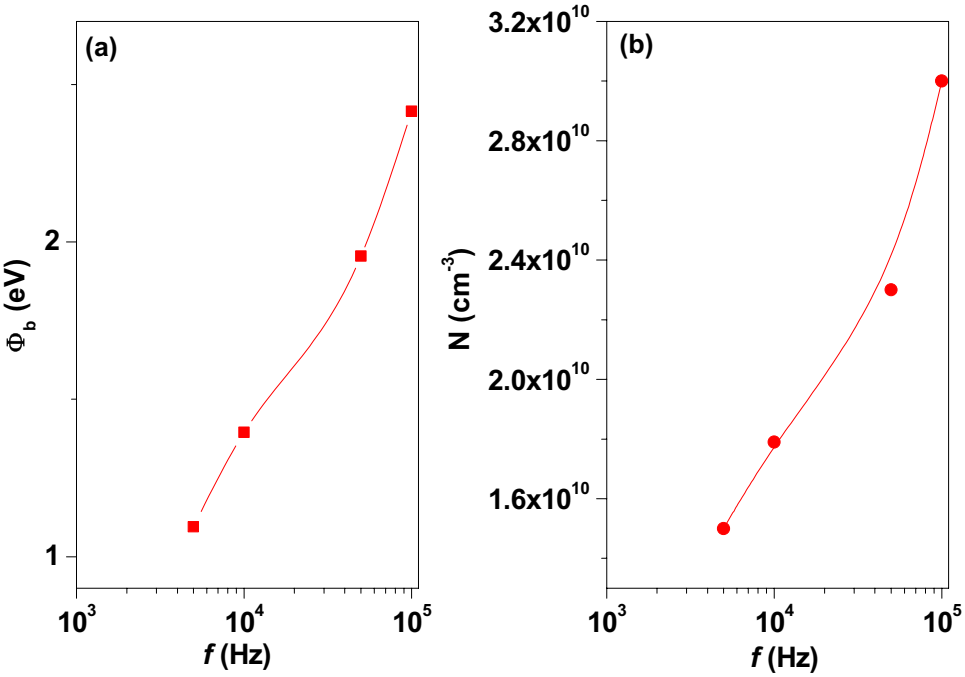

Fig. 13 **a** Plot of the barrier height, Φ_b vs. f and **b** plot of the carrier concentration, N vs. f for Rh.B/p-Si heterojunction

where ε is the dielectric constant, ε_o is the permittivity of free space, A is the area, N is the carrier concentration, V_b is the built-in potential, V is the reverse biasing. The value of the extraction of the barrier height can be achieved using the following relationship:

$$\Phi_b = V_b + V_F + \left(\frac{kT}{q}\right), \tag{5}$$

where V_F is the difference of energy between Fermi level and valence band edge for the semiconductors of p-type. In addition, the maximum electric field as a function of built-in potential can be given by the following expression, where E_{max} is the maximum electric field and given by

$$E_{max} = \left(\frac{2qNV_b}{\varepsilon}\right)^{1/2}. \tag{6}$$

Figure 13a, b shows the frequency dependence for both Φ_b and N in the frequency range 5–100 kHz. As expected, an increase of Φ_b with increasing frequency is inconsistent with those published in the literature by Osiris et al. [18]. However, another observation for the results is the higher value of the barrier height deduced from capacitance–voltage measurements as compared with those obtained from the measurements of current density–voltage. This behavior can be can be ascribed to the inhomogeneity of the barrier height at the heterojunction interface [50]. In addition, N increases with increasing the applied frequency which can be due to the partial contribution of the interface state charges in the device capacitance [51, 52]. Figure 14a, b shows the frequency dependence of E_{max} and the width of the depletion region (W) in the frequency range from 5 to 100 kHz. As observed, E_{max} increases, while W decreases with increasing frequency. This frequency dependence is correlated with the effect of a series resistance on these characteristics and the non-uniformity of the interfacial insulator layer thickness [50].

3.5 Energy band diagram

The energy band diagram of Rh.B/p-Si heterojunction is demonstrated in Fig. 15. This figure demonstrates the energy levels graph of the valence and conduction bands (p-Si), comparing with HOMO and LUMO levels of Rh.B which ought to be adjusted through the association. The Rh.B film builds a barrier with p-Si for the charge-carrier transportation throughout the interface. Every one of the information in the schematic graph is acquired from the current and capacitance–voltage characteristics as considered in the literature [53, 54].

4 Conclusions

The spin-coated Rh.B thin film shows amorphous nature and nanostructure characteristics. The optical absorption characteristics confirm an indirect allowed transition with an energy band gap of 2.1 eV and Urbach energy of 29 meV. The electrical characteristics of Rh.B/p-Si heterojunctions were investigated by I–V and C–V characteristics. The I–V measurements illustrated the nonlinear characteristics due to

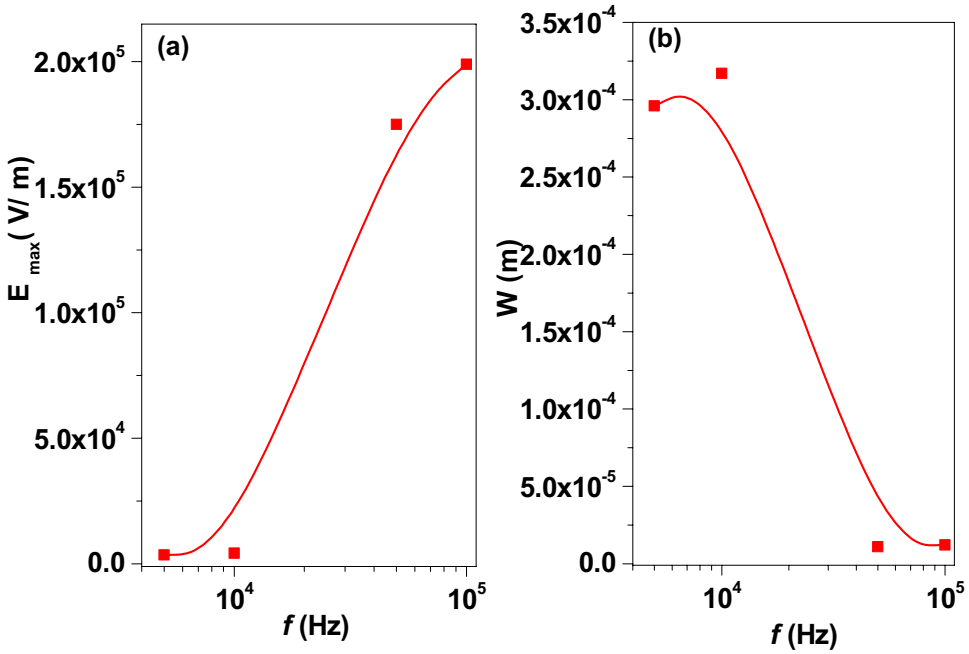

Fig. 14 **a** Plot of E_{max} vs. f and **b** plot of W vs. f for Rh.B/p-Si heterojunction

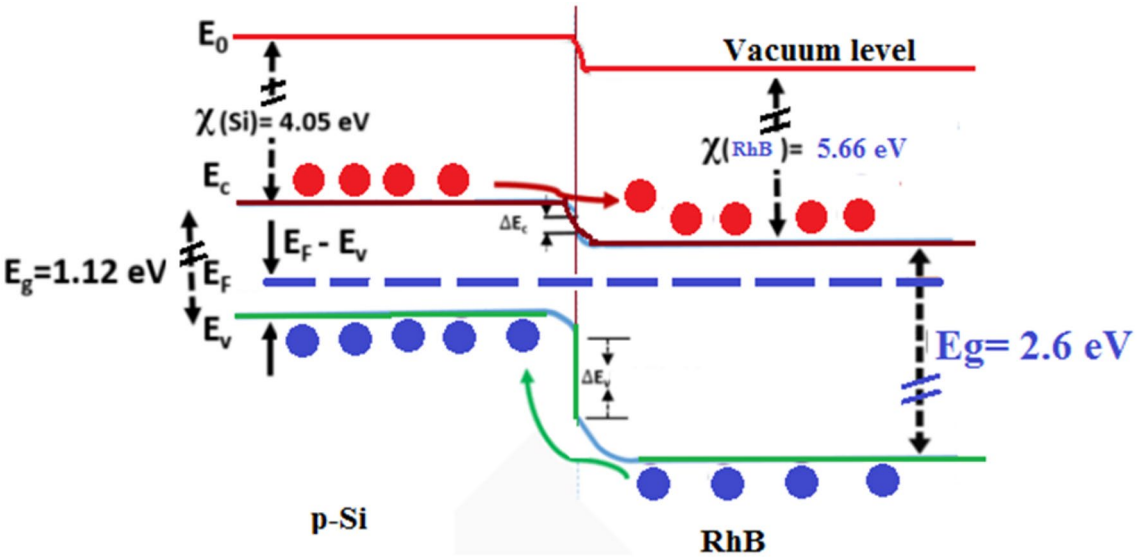

Fig. 15 Energy band diagram of Rh.B/p-Si heterojunction

the influence of series and shunted resistances at the higher and lower applied voltage region, respectively. Values of ideality factor, barrier height, and series resistance were extracted using Cheung–Cheung functions. The analysis of the *I–V* characteristics confirms the presence of two predominant conduction mechanisms depending on the range of applied voltage. Capacitance and conductance measurements showed a remarkable sensitivity for the applied voltage and frequency, particularly at the lower frequency range. The behavior of both *C–V* and *G–V* can be due to the distribution of interface states at the interface and the effect of series resistance. Frequency and voltage-dependent of series resistance can be due to enough energy for the trap charges to deliverance at the interface. Accordingly, the studied Rh.B/p-Si heterojunction can be employed as a kindly electronic material in various electronic device applications.

Acknowledgements The authors express their appreciation to "The Research Center for Advanced Materials Science (RCAMS)" at King

Khalid University for funding this work under Grant number RCAMS/KKU/003-18. Moreover, the authors would like to thank Dr. Shiamaa Abdel Halim for providing the molecular calculations.

References

1. W. Hu, *Organic optoelectronics* (Wiley-VCH Verlag GmbH & Co. KGaA, Boschstr, Weinheim, 2013)
2. W. Brütting, C. Adachi, *Physics of organic semiconductors* (Wiley-VCH Verlag & Co. KGaA, Boschstr, Weinheim, 2012)
3. S. Rao, N. Srinivas, D. Rao, L. Giribabu, B. Maiya, R. Philip et al., Opt. Commun. **182**, 255–264 (2000)
4. A. Gilman, A. Drachev, High Energy Chem. **40**, 70–78 (2006)
5. Z.V. Vardeny, A.J. Heeger, A. Dodabalapur, Synth. Met. **148**, 1–3 (2005)
6. M.M. Abutalib, M. Shkirb, I.S. Yahia, S. AlFaify, A.M. El-Naggar, V. Ganesh, Optik **127**, 6601–6609 (2016)
7. S.R. Forrest, Nature **428**, 911–918 (2004)
8. H. Sirringhaus, Adv. Mater **17**, 2411–2425 (2005)
9. Y. Guo, G. Yu, Y. Liu, Adv. Mater **22**, 4427–4447 (2010)
10. T.N. Ng, B. Russo, B. Krusor, R. Kist, A.C. Arias, Org. Electron. **12**, 2012–2018 (2011)
11. Y. Diao, B.C. Tee, G. Giri, J. Xu, D.H. Kim, H.A. Becerril, R.M. Stoltenberg, T.H. Lee, G. Xue, S.C. Mannsfeld, Nat. Mater. **12**, 665–671 (2013)
12. S. Kazemifard, L. Naji, F. Afshar Taromi, J. Coll. Interf. Sci. **515**, 139–151 (2018)
13. A.A.M. Farag, I.S. Yahia, Opt. Commun. **283**, 4310–4317 (2010)
14. A.A.M. Farag, I.S. Yahia, Synth. Met. **161**, 32–39 (2011)
15. C. Zhan, J.A. Nichols, D.A. Dixon, J. Phys. Chem. A **107**, 4184–4195 (2003)
16. J. Tauc, *Amorphous and Liquid Semiconductors* (Plenum, New York, 1974)
17. A. Alaa, S.A. Akl, Mahmoud, Optik **172**, 783–793 (2018)
18. W.G. Osiris, A.A.M. Farag, I.S. Yahia, Synth. Met. **161**, 1079–1087 (2011)
19. A.A.M. Farag, I.S. Yahia, T. Wojtowicz, G. Karczewski, J. Phys. D Appl. Phys. **43**, 215102 (2010)
20. C. Thanachayanont, K. Import, S. Sahasithiwat, J. Korean Phys. Soc. **52**, 1540–1544 (2008)
21. M.E. Aydin, A.A.M. Farag, M. Abdel-Rafea, A.H. Ammar, F. Yakuphanoglu, Synth. Met. **161**, 2700–2707 (2012)
22. A.A.M. Farag, W.G. Osiris, A.H. Ammar, Appl. Surf. Sci. **259**, 600–609 (2012)
23. A.A.M. Farag, M.S. Sawsan, M.E. Haggag, Mahmoud, Spectrochimica Acta Part A **93**, 116–124 (2012)
24. G. Ersöz, İ Yücedağ, S. Bayrakdar, Ş Altındal, A. Gümüş, J. Mater. Sci. **28**, 6413–6420 (2017)
25. F. Yakuphanoglu, M. Kandaz, B. Filiz Senkal, Sensors Actuators **153**, 191 (2009)
26. N. Oyama, S. Kaneko, K. Momiyama, K. Kanomata, F. Hirose, Microelectron. Eng **104**, 130–134 (2013)
27. D.S. Reddy, M.B. Reddy, N.N.K. Reddy, V.R. Reddy, J. Mod. Phys. **2**, 113–123 (2011)
28. W. Khan, S. Kim, Mater. Sci. Semicond. Proc. **66**: 232–240 (2017)
29. N.M. Khusayfan, A.A. Al-Ghamdi, F. Yakuphanoglu, J. Alloys Compd. **663**, 796–807 (2016)
30. A.R. Deniz, Z. Çaldıran, M. Biber, Ü. İncekara, Ş. Aydoğan, J. Alloys Compd. **763**, 622–628 (2018)
31. T. Kiuru, A.V. Räisänen, IEEE Trans. Microw. Theory Techn. **59**, 2108–2116 (2011)
32. S.H. Phark, H. Kim, K.M. Song, D.-W. Kim, J. Korean Phys. Soc. **58**, 1356–1360 (2011)
33. J.H. Werner, H.H. Guttler, J. Appl. Phys. **69**, 1522–1533 (1991)
34. F. Yakuphanoglu, W.A. Shah, M. Farooq, Acta Phys. Pol. **120**, 558–562 (2011)
35. J. Xu, Z. Jia, N. Zhang, T. Ren, J. Appl. Phys. **111**, 074101 (2012)
36. G. Ersöz, İ Yücedağ, S. Bayrakdar, Ş. Altındal, A. Gümüş, J. Mater. Sci. Electron. **28**, 6413–6420 (2017)
37. S.M.S. Haggag, A.A.M.Farag, M. Abdelrafea, Spectrochim. Acta A **110**, 14–19 (2013)
38. Y. Xia, W. He, L. Chen, X. Meng, Z. Liu, Appl. Phys. Lett. **90**, 022907 (2007)
39. B.T. Phan, C. Jung, T. Choi, J. Lee, J. Korean Phys. Soc **51**, 664–668 (2007)
40. M. Taukeer Khan, V. Agrawal, A. Almohammedi, V. Gupta, Solid-State Electron. **145**, 49–53 (2018)
41. M. Abkowitz, J.S. Facci, J. Rehm, J. Appl. Phys. **83**, 2670–2676 (1998)
42. E.H. Nicollian, A. Goetzberger, Appl. Phys. Lett. **7**, 216–220 (1965)
43. M. Soylu, A.A. Al-Ghamdi, W.A. Farooq, F. Yakuphanoglu, Microelectron. Eng. **154**, 26–37 (2016)
44. S. Zeyrek, E. Acaroglu, S. Altındal, S. Birdogan, M.M. Bülbül, Curr. Appl. Phys. **13**, 1225–1230 (2013)
45. M.M. Bülbül, S. Zeyrek, Microelectron. Eng **83**, 2522–2526 (2006)
46. S.M. Sze, *Physics of Semiconductor Devices*, Second edn. (Wiley, New York, 1981)
47. A.M. Goodman, J. Appl. Phys. **34**, 329–338 (1963)
48. J.J. Low, M.L. Kreider, D.P. Pulsifer Andrew, S. Jones, T.H. Gilani, Am. Undergraduate Res. **7**, 27–32 (2008)
49. S.J. Fonash, J. Appl. Phys. **54**, 1966–1975 (1983)
50. S. Aydogan, M. Saglam, A. Turut, Polymer **46**, 563–568 (2005)
51. A. Tataroglu, S. Altindal, Microelectron. Eng. **83**, 582–588 (2006)
52. A. Tataroglu, S. Altindal, Microelectron. Eng. **85**, 2256–2260 (2008)
53. J. Liang, T. Miyazaki, M. Morimoto, S. Nishida, N. Shigekawa, J. Appl. Phys **114**, 183703 (2013)
54. A.G. Jadhav, L. Rhyman, I.A. Alswaidan, P. Ramasami, N. Sekar, Comp. Theor. Chem. **1131**, 1–12 (2018)